Volume 12
Number 14
14 April 2024
Pages 4907–5258

Journal of Materials Chemistry C

Materials for optical, magnetic and electronic devices

rsc.li/materials-c

ISSN 2050-7526

ROYAL SOCIETY OF CHEMISTRY

PAPER

Dirk Volkmer, Gregor Kieslich *et al.*
Spin-state dependent pressure responsiveness of Fe(II)-based triazolate metal–organic frameworks

Journal of Materials Chemistry C

ROYAL SOCIETY OF CHEMISTRY

PAPER

View Article Online
View Journal | View Issue

Cite this: J. Mater. Chem. C, 2024, 12, 4954

Spin-state dependent pressure responsiveness of Fe(II)-based triazolate metal–organic frameworks†

Silva M. Kronawitter, ‡[a] Richard Röß-Ohlenroth, ‡[b] Sebastian A. Hallweger, [a] Marcel Hirrle,[b] Hans-Albrecht Krug von Nidda,[c] Tobias Luxenhofer,[b] Emily Myatt, [d] Jem Pitcairn, [d] Matthew J. Cliffe, [d] Dominik Daisenberger, [e] Jakub Wojciechowski,[f] Dirk Volkmer *[b] and Gregor Kieslich *[a]

Received 29th January 2024,
Accepted 20th February 2024

DOI: 10.1039/d4tc00360h

rsc.li/materials-c

Fe(II)-containing Metal–Organic Frameworks (MOFs) that exhibit temperature-induced spin-crossover (SCO) are candidate materials in the field of sensing, barocalorics, and data storage. Their responsiveness towards pressure is therefore of practical importance and is related to their longevity and processibility. The impact of Fe(II) spin-state on the pressure responsiveness of MOFs is yet unexplored. Here we report the synthesis of two new Fe(II)-based MOFs, *i.e.* $Fe(cta)_2$ ($(cta)^-$ = 1,4,5,6-tetra hydrocyclopenta[*d*][1,2,3]triazolate) and $Fe(mta)_2$ ($(mta)^-$ = methyl[1,2,3]triazolate), which are both in high-spin at room temperature. Together with the isostructural MOF $Fe(ta)_2$ ($(ta)^-$ = [1,2,3]triazolate), which is in its low-spin state at room temperature, we apply these as model systems to show how spin-state controls their mechanical properties. As a proxy, we use their bulk modulus, which was obtained *via* high-pressure powder X-ray diffraction experiments. We find that an interplay of spin-state, steric effects, void fraction, and absence of available distortion modes dictates their pressure-induced structural distortions. Our results show for the first time the role of spin-state on the pressure-induced structural deformations in MOFs and bring us a step closer to estimating the effect of pressure as a stimulus on MOFs *a priori*.

Introduction

Metal–organic frameworks (MOFs) are built from inorganic metal nodes and multitopic organic linkers, providing a large chemical parameter space for synthesising materials with targeted functionalities. On the most fundamental level, designing material functionality means control over the materials' responsiveness to stimuli such as pressure, temperature, electric and magnetic fields, and chemical triggers *via* composition and structure.[1,2]

In this work, we focus on hydrostatic pressure as a stimulus. In 2008, it was proposed that "[The MOFs'] well documented structural complexities can be expected to yield unprecedented pressure-induced phenomena".[3] High-pressure research on MOFs over the past 15 years has fulfilled these expectations, revealing a variety of fascinating phenomena. Examples include pressure-induced structural flexibility with large volume changes as interesting for damping, shock absorbers, and mechanical energy storage;[4–6] large negative linear compressibility as a potential starting point for new actuating technologies,[7,8] pressure-induced postsynthetic modification reactions of the metal node,[9] and defect-dependent material stabilities[10] with implications for material processing parameters.

As MOFs move closer to practical use, their mechanical properties such as bulk modulus (B), or their compressibility as the inverse, hardness, Young's modulus, and stress stability are attracting increasing attention.[11–14] Learning about the relationships between chemical composition, structure, and macroscopic mechanical properties, will allow these properties to be targeted synthetically. In this context, B, and its linear components, as a measure of the resistance of a MOF to hydrostatic pressure are important parameters. These parameters are tied to interatomic potentials and the inner energy of a crystal structure.[15] Therefore, they are important measures of how the MOF's crystal chemistry as a whole, *i.e.* chemical

[a] Technical University of Munich, TUM Natural School of Sciences, Lichtenbergstr. 4, Garching 85748, Germany. E-mail: gregor.kieslich@tum.de
[b] Chair of Solid State and Materials Chemistry, Institute of Physics, University of Augsburg, Universitätsstr. 1, Augsburg 86159, Germany. E-mail: dirk.volkmer@physik.uni-augsburg.de
[c] Experimental Physics V, Center for Electronic Correlations and Magnetism, Institute of Physics, University of Augsburg, Universitätsstr. 1, Augsburg 86159, Germany
[d] School of Chemistry, University of Nottingham, Nottingham NG7 2RD, UK
[e] Diamond Light Source Ltd., Diamond House, Harwell Campus, Didcot OX11 ODE, UK
[f] Rigaku Europe SE, Hugenottenallee 167, Neu-Isenburg, Germany

† Electronic supplementary information (ESI) available. CCDC 2311804–2311811. For ESI and crystallographic data in CIF or other electronic format see DOI: https://doi.org/10.1039/d4tc00360h

‡ Shared contribution.

bond strength, nature of chemical bonds, connectivity, available pore space, and defect chemistry together determine its pressure responsiveness.

Over the past years, a few important principles between a MOF's crystal chemistry and B have been discovered.[12,16,17] For instance, in a comprehensive study by K. Chapman and O. Farha on isoreticular MOF series with **fcu** and **scu** topology, a relation between void fraction, linker length, and B has been established.[18] It has been found that within an isoreticular MOF series, a larger void space (longer linkers) correlates to a reduction of B. Moreover, it has been pointed out that MOFs with rotated and out-of-plane bended linker molecules such as DUT-52 (B = 17(2) GPa) and PCN-57 (B = 4.6(1) GPa) show a significantly smaller B when compared to their isoreticular counterparts with linear linkers (B between 21.1(6) and 37.9(6) GPa). This finding suggests that pre-distorted linkers introduce preferred low-energy pathways for structural distortion as a response to hydrostatic pressure. Furthermore, it has been shown for NU-901 that post-synthetic incorporation of a linker between two open metal-sites, a process known as retrofitting,[19] increases B.[20] This result agrees with intuition and with recent results from computation where a positive correlation between metal-node connectivity and B has been found.[21] Additionally, it has been discovered that the coordination bond strength between the linker and the metal-node[22] and the concentration of point defects influences B.[10] Importantly, both factors also influence the critical pressure where pressure-induced amorphisation occurs.[23] There has been interest in the pressure-dependent spin-state of MOF-related Hoffman-type clathrates[24–26] and the elastic properties of molecular Fe(II) SCO complexes,[27,28] highlighting that changing the spin-state significantly impacts B. The impact of the spin-state of metal centres within the metal-node on the mechanical properties of MOFs has not been explored to our knowledge. Knowing about the role of coordinative bond strength in determining B, it can be anticipated that the metal-centre spin-state, which comes with a change in coordination bond length and strength, will significantly impact the material response to hydrostatic pressure.

$Fe(ta)_2$ is a MOF with thermal SCO, $(ta)^-$ = 1,2,3-triazolate.[29] $Fe(ta)_2$ belongs to a larger family of isostructural MOFs, $M(ta)_2$ (with M^{2+} = Cu^{2+}, Cd^{2+}, $Cr^{2+/3+}$, Mn^{2+}, Co^{2+}, Zn^{2+}, and Mg^{2+}),[30–34] where the divalent metal centres are octahedrally coordinated by μ_3-bridging 1,2,3-triazolate ligands to form a 3D network with two crystallographically independent Fe(II) sites, see Fig. 1. Notably, the underlying topology is of type **dia**, or when treating both Fe(II) sites independently, parallels to the structure of β-cristobalite can be drawn. Initially, $Fe(ta)_2$ has high intrinsic electrical conductivity of 7.7×10^{-5} S cm^{-1},[30] which is sensitive towards gas pressure[35] and can be further increased upon partial oxidation of metal centres *via* I_2 or thianthrenium tetrafluorborate.[36] More recently, $Fe(ta)_2$ has been shown to exhibit a large hysteresis SCO in a bistable region between 320 °C (heating) and 185 °C (cooling), associated with a change of unit cell volume of approximately 22%, while retaining its structural connectivity and cubic symmetry.[37] Notably, the SCO

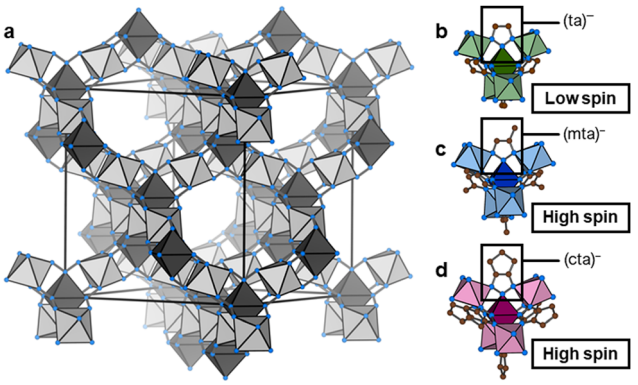

Fig. 1 (a) Schematic of the isostructural **dia**-type network of Fe(II)-containing MOFs investigated in this work. The modification in $Fe(mta)_2$ and $Fe(cta)_2$ has a significant impact on the void fraction which is reduced in $Fe(mta)_2$ and $Fe(cta)_2$ when compared to $Fe(ta)_2$. In (b–d) a visualisation of metal nodes of $Fe(ta)_2$ (b), $Fe(mta)_2$ (c), and (d) $Fe(cta)_2$ is shown, where the colour-code highlights the different coordinating triazolate ligands used in this work. For visualisation purposes, disorder of the $-CH_3$ group of $(mta)^-$ is not shown in (c). Likewise, H atoms were deleted for clarity. Colour-code: brown spheres – carbon, blue spheres – nitrogen; different colour saturations of polyhedrons indicate the two crystallographically independent Fe(II) sites.

comes with a significant change in Fe–N bond lengths (Δd = 0.18–0.21 Å), which accounts for the changes in unit cell volume. Long-range cooperativity was recently found to be responsible for the large hysteresis of the SCO in $Fe(ta)_2$.[38]

Drawing inspiration from the extensive work on Fe(II)-containing SCO compounds such as Hofmann-type clathrates and molecular complexes,[39] we expect that chemical modification of the $(ta)^-$ backbone impacts the critical temperature of the SCO transition. For our purpose, *i.e.* the study of Fe(II) spin-state on the pressure response, we seek to decrease the SCO temperature below room temperature while maintaining the overall connectivity and cubic symmetry of the material. Together with $Fe(ta)_2$, such a compound would provide a model system for studying the impact of Fe(II) spin-state on the compressibility.

Here we report the synthesis of $Fe(cta)_2$ ($(cta)^-$ = 1,4,5,6-tetra hydrocyclopenta[*d*][1,2,3]triazolate) and $Fe(mta)_2$ ($(mta)^-$ = methyl [1,2,3]triazolate), two new Fe(II)-based MOFs that are in their high-spin state at room temperature. We apply $Fe(cta)_2$ as model system for exploring the impact of spin-state on the pressure response of Fe(II) containing MOFs *via* high-pressure powder X-ray diffraction (HPPXRD). It is shown that $Fe(ta)_2$ and $Fe(cta)_2$ exhibit similar B which is ascribed to the difference in void fraction and Fe–N bond strengths as counteracting effects. The results advance our understanding of the crystal chemical factors that contribute to the mechanical properties of MOFs, knowledge that is of increasing importance when considering their potential as working media in barocalorics[40] and mechanical energy storage.[41]

Results and discussion

Material synthesis and characterisation

$Fe(ta)_2$ was synthesised by following a previously established route,[29,35] and similar procedures were used for the synthesis of

$Fe(cta)_2$ and $Fe(mta)_2$, see ESI† for synthetic details (S-2). We would like to mention that H-ta (1*H*-1,2,3-triazole) is commercially available, while H-cta (1,4,5,6-tetrahydrocyclopenta-1*H*-1,2,3-triazole) and H-mta (4-methyl-1*H*-1,2,3-triazole) were synthesised by following adapted synthetic procedures from the literature, see ESI† for details (S-2).[42,43] After synthesis of the MOFs, IR spectroscopy was performed, where signals from stretch vibrations of cyclopentyl and methyl hydrogen atoms between 2800–3000 cm^{-1} confirm the presence of (chemically modified)-triazolate linkers in the obtained powders (Fig. S2, ESI†). To remove potential residual *N*,*N*-dimethylformamide (DMF), $Fe(cta)_2$ and $Fe(mta)_2$ were washed with methanol (MeOH) and dried *in vacuo* at room temperature (for $Fe(cta)_2$) or at 280 °C (for $Fe(mta)_2$). Thermogravimetrical analysis (TGA) and differential scanning calorimetry (DSC) of $Fe(cta)_2$ and $Fe(mta)_2$ show that both compounds exhibit a relatively high thermal stability with a decomposition onset at approximately 670 K (Fig. S4 and S5, ESI†). This is slightly higher than previously observed for $Fe(ta)_2$, where decomposition processes start at approximately 613 K.[29] Similarly to $Fe(ta)_2$, no evidence for the release of solvent molecules from potential void space was observed for both compounds (Fig. S3–S5, ESI†).

Since the applied synthetic route led to crystalline powders of $Fe(ta)_2$, $Fe(cta)_2$, and $Fe(mta)_2$, powder X-ray diffraction (PXRD) was used for structure analysis, see ESI† for details (Fig. S13, S16, and Table S3). In an initial step, the synthesis of phase pure $Fe(ta)_2$ was confirmed *via* a Pawley profile fit analysis, and subsequently, atomic positions were obtained by Rietveld refinements (Fig. 2(a) and Fig. S22, ESI†). $Fe(ta)_2$ was refined in the previously reported cubic structure, space-group $Fd\bar{3}m$ (a = 16.5969 Å). The obtained Fe–N bond lengths (Fe1–N1 = 1.9736 Å and Fe2–N2 = 1.99082 Å) are indicative for Fe(II) centres in their low-spin state, which agree with the literature.[29] Visual comparison of all PXRD pattern suggests that $Fe(ta)_2$, $Fe(cta)_2$, and $Fe(mta)_2$ are isostructural MOFs, which was confirmed *via* Rietveld-based structure refinement, see ESI† for refinement details (Fig. 2 and Fig. S16, S-19–S-21).

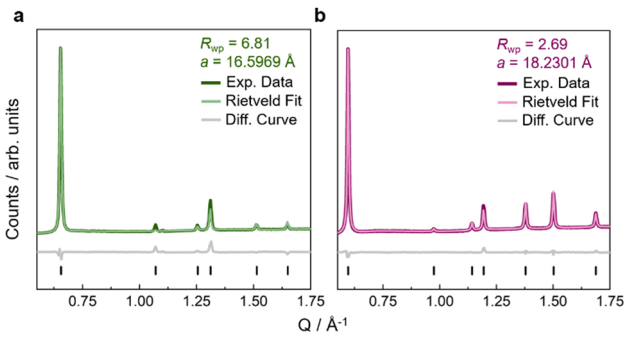

Fig. 2 Rietveld refinements against high-resolution PXRD pattern at ambient pressure of $Fe(ta)_2$ (a) in green and $Fe(cta)_2$ (b) in purple. Experimental data is shown as dark line, the calculated data from Rietveld refinement as light line, and the difference curve (fit – data) as grey line. Reflection positions are shown as black vertical tick marks. Rietveld fit of $Fe(mta)_2$ is given in the ESI† (Fig. S20).

The structures of $Fe(cta)_2$ and $Fe(mta)_2$ were refined in the cubic space-group $Fd\bar{3}m$ with lattice parameters of a = 18.2301 Å ($Fe(cta)_2$) and a = 17.3175 Å ($Fe(mta)_2$) (Fig. 2). Compared to $Fe(ta)_2$ (Fig. S20, ESI†), where Fe(II) centres are in their low-spin state at room temperature, the observed Fe–N bond lengths of $Fe(cta)_2$ and $Fe(mta)_2$ (*i.e.* Fe(II)–N > 2.0 Å) indicate that both compounds are in their high-spin state. This was confirmed by variable temperature magnetic susceptibility measurements in the temperature range between 2 and 700 K of all compounds, see ESI† for detailed data interpretation (Fig. S9 and S-12). To further verify structure refinement from PXRD data, 3D electron diffraction (3DED) at variable temperatures between 173 and 373 K was applied for structure solution from small crystallites, for experimental details and crystallographic outcomes see ESI† (Tables S8, S9 and Fig. S35–S38). The 3DED structures at room temperature, including bond distances and lattice parameters of the high-spin MOFs $Fe(cta)_2$ (Fe1–N1 = 2.223(18) Å, Fe2–N2 = 2.231(15) Å, and a = 18.19(10) Å) and $Fe(mta)_2$ (Fe1–N1 = 2.198(15) Å, Fe2–N2 = 2.117(14) Å, and a = 17.26(9) Å), are in close agreement to the results from the Rietveld analysis.

Therefore, the backbone modification of the triazolate linker impacts the critical temperature of the SCO effect and its nature. With increasing bulkiness of the chemical modification, *i.e.* $(ta)^-$ < $(mta)^-$ < $(cta)^-$, the SCO temperature decreases and suppresses hysteretic behaviour. By drawing parallels to molecular SCO complexes,[44] this is rationalised by steric effects which provide an energy penalty for compression of the frameworks into the low-spin state. Especially in the high-spin $Fe(cta)_2$ framework, opposing hydrogen atoms of the $(cta)^-$ ligands are already in a repulsive range, with distances of H7A–H7A 2.1008(82) Å and H6A–H6A 2.1763(85) Å when looking at the 3DED data. In $Fe(mta)_2$, the larger distances between the methyl groups allow for more flexibility, although their steric demand still results in a significant shift of the phase transition to lower temperatures, as well as a two-step transition behaviour. Moreover, residual DMF trapped in the voids of the as-synthesised $Fe(mta)_2$-as seems to contribute to the steric crowding, causing a smeared-out transition at lower temperatures (Fig. S6, S7 and S9, ESI†). In addition, we calculated the void fraction of all three materials *via* Platon[45] (SOLV option), see Table 1. As expected, chemical modification of the $(ta)^-$ backbone in $Fe(cta)_2$ significantly decreases the existing void fraction compared to $Fe(ta)_2$, which can be expected to significantly influence the materials' pressure responsiveness.

Overall, a series of isostructural triazole-based Fe(II) MOFs is obtained where Fe(II) centres are in different spin-states at ambient conditions. These represent a good model series to study the impact of spin-state on their pressure response. An overview of structural and magnetic data of $Fe(ta)_2$ and $Fe(cta)_2$ is given in Table 1 and full crystallographic data, including details of structure refinement is given in the ESI.†

High-pressure structural response

With the isostructural series of $Fe(ta)_2$, $Fe(cta)_2$, and $Fe(mta)_2$ on hand, we used HPPXRD to investigate the impact of varying spin-state of Fe(II) on the MOF's response to hydrostatic

Table 1 Overview of structural and magnetic data for $Fe(ta)_2$ and $Fe(cta)_2$. *B*s were calculated by using the 2nd B–M equation of states fits *via* EOSFit. Because of the pressure-induced phase transition in $Fe(mta)_2$, no *B* was calculated. Void fractions were calculated in PLATON (using SOLV option) based on the Rietveld refined structures in this work. The Fe(II)–N bond distances were derived from Rietveld refinement. The calculated void fraction of $Fe(ta)_2$ including bond distances is in good agreement with previous structural reports (*26.2% – CCDC 837468 and 27.6% – CCDC 1963573)

MOF	$Fe(ta)_2$	$Fe(cta)_2$
Spin-state	Low-spin	High-spin
Void fraction/%*	25.8	5.9
Fe(II)–N/Å	1.9736(Fe1–N1)	2.15631(Fe1–N1)
	1.99082(Fe2–N2)	2.09172(Fe2–N2)
B/GPa	28.2 ± 0.2	29.5 ± 0.5

pressure as a stimulus. HPPXRD was performed at beamline I15 at the Diamond Light Source (DLS, UK). For obtaining an excellent pressure resolution of our $V(p)$ datasets, which is critical for obtaining accurate *B*s, we have applied the "high-pressure jump cell".[46] This is a custom-made high-pressure cell that enables HPPXRD measurements up to p_{max} = 0.4 GPa with defined pressure increments of Δp = 0.02 GPa (Fig. 3), see ESI† for the measurement of a standard material (S-32). Silicone oil AP-100 was used as a pressure transmitting medium (PTM), which has previously been applied for HPPXRD experiments of Zr-based MOFs[47] and molecular perovskites.[48] To the best of our knowledge, silicone oil AP-100 acts as hydrostatic, non-penetrating PTM, enabling to study the mechanical response of the MOFs without any additional effects such as penetration of the PTM into the pores of the MOF.[3,49]

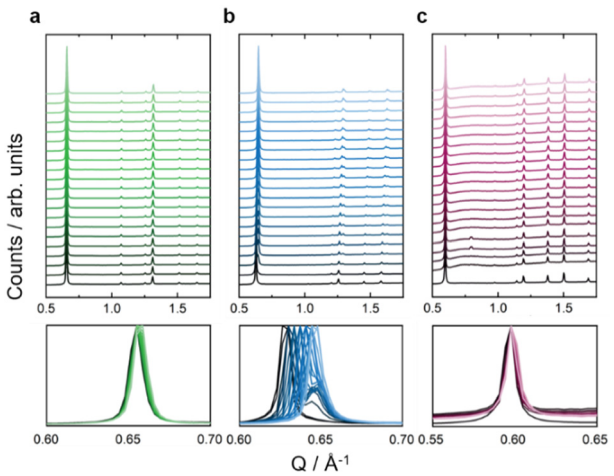

Fig. 3 Stacked HPPXRD pattern (λ = 0.4246 Å) of (a) $Fe(ta)_2$ in green, (b) $Fe(mta)_2$ in blue, and (c) $Fe(cta)_2$ in purple. The HPPXRD pattern were collected between ambient pressure (bottom) and 0.4 GPa (top) with the step size of Δp = 0.02 GPa. For visualisation purposes, the data was normalised to the (111) reflection. The bottom panel focus on the peak of the reflection of the (111) plane, showing a gradual shift for $Fe(ta)_2$ and $Fe(cta)_2$. For $Fe(mta)_2$ an additional peak is observed starting from approximately p_{crit} = 0.04 GPa which is ascribe to a pressure-induced phase transition that is incomplete at p_{max}.

From visual inspection of HPPXRD data (Fig. 3), none of the studied MOFs exhibits pressure-induced amorphisation up to 0.4 GPa.[50] The analysis of the full-width at half maximum (fwhm) of the applied peak profile function of $Fe(ta)_2$ and $Fe(cta)_2$ confirms this observation (Fig. S26, ESI†). For $Fe(mta)_2$, a pressure-induced phase transition complicates such an analysis, see below. This is expected since only a few MOFs, such as UiO-66 with a large concentration of point defects,[10] and DMOF-1 with non-functionalized benzendicarboxylate linkers,[51] have been reported to irreversibly amorphise at hydrostatic pressures below $p < 0.4$ GPa. Please note, that amorphisation under non-hydrostatic compression is known to occur significantly earlier, as reported for ZIF-8 and MOF-5.[50,52] Upon increasing pressure, a peak shift is observed for $Fe(ta)_2$, $Fe(cta)_2$, and $Fe(mta)_2$, showing structural compression (Fig. 3). For $Fe(ta)_2$ and $Fe(cta)_2$ no evidence for a phase transition is observed, while $Fe(mta)_2$ undergoes a pressure-driven phase transition at approximately p_{crit} = 0.04 GPa. This can be expected due to the temperature dependent SCO just below room temperature. Therefore, $Fe(ta)_2$ and $Fe(cta)_2$ were selected as model systems to learn about the impact of spin-sate on the pressure responsiveness. $Fe(mta)_2$ with its pressure-induced phase transition and open questions related to its ambient crystal structure, see S-43 (ESI†), displays a more complex case and will be addressed independently in a follow-up study. HPPXRD data of $Fe(ta)_2$ and $Fe(cta)_2$ have been analysed *via* Pawley profile fits and Rietveld-based structural refinements for extracting lattice parameters (a), volumes (V) and atomic positions as well as Fe–N bond length as a function of pressure, providing complete $V(p)$ data sets up to p_{max} for both samples, see ESI† for a full list of Pawley profile fit results, *i.e.* lattice parameters, R_{wp} values, and fwhm (Tables S4, S5 and Fig. S21, S26).

For describing the mechanical resistance of $Fe(ta)_2$ and $Fe(cta)_2$ against pressure as a stimulus, we focus on *B* as the inverse of the material's compressibility. *B*s were calculated by fitting a Birch–Murnaghan (B–M) equation of state to the $V(p)$ data up to p_{max} = 0.4 GPa by using both second and third order B–M equation of state fits *via* EoSFit7-Gui (Table 1), see ESI† for details (Fig. S27 and S28).[53] Similar results were obtained by using PASCal[54] (Table S8, ESI†). We would like to note that for both methods, *i.e.* EOSFit and PASCal, only 2nd order B–M fits show standard errors (σB) in the range of the measured reference material (S-32, ESI†) and are used for further discussion.

For both MOFs, we obtain similar *B*s, $B(Fe(ta)_2)$ = 28.2 ± 0.2 GPa and $B(Fe(cta)_2)$ = 29.5 ± 0.5GPa. Compared to other prototypical MOFs such as UiO-66(Zr) (B = 37.9(6) GPa),[18] HKUST-1 (B = 30 GPa)[3], ZIF-4(Zn) (B = 2–4.4 GPa),[55] and ZIF-8 (B = 6.5 GPa),[50] $Fe(ta)_2$ and $Fe(cta)_2$ can be considered relatively rigid or rather 'hard MOFs'.[56] To rationalise these values, we anticipate that the absence of a clear pressure-induced low-energy distortion pathway in the structures of $Fe(ta)_2$ and $Fe(cta)_2$ is key. Example for such pathways are pressure-induced wine-rack type network motions as observed in MOFs such as MIL-53(Al) ($Al[O_2C–C_6H_4–CO_2]OH$)[57] and Cu_2(DB-bdc)$_2$dabco (DB-bdc = 2,5-dibutoxy-1,4-benzendicarboxylate, dabco = 1,4-diazabicyclo[2.2.2]octane)[51] and MOFs with predistorted linkers such as DUT-52 and PCN-57.[18] The structures of $Fe(ta)_2$ and $Fe(cta)_2$ are

related to the structure of β-cristobalite, where temperature and pressure are known to activate tilts of polyhedra,[58,59] however, the μ_3-connectivity of 1,2,3-triazolate ligands makes similar distortions in $Fe(ta)_2$ and $Fe(cta)_2$ energetically unfavourable. Therefore, any pressure-induced structural deformation is coupled to bond-length compression and linker bending, where the latter becomes energetically favoured by void space, which reduces steric hindrance. The same argumentation applies to UiO-66(Zr) and HKUST-1, where presumably the metal-node coordination number is the dominating structural feature in defining *B*. This train of thought agrees with the observation that increasing the length of the linker leads to a reduction of *B* as previously shown for UiO-66(Zr) (B = 37.9(6) GPa) and UiO-67(Zr) (B = 21.1(6) GPa).[18]

Looking more specifically at the comparison of $Fe(ta)_2$ and $Fe(cta)_2$, the difference in the void fraction of $Fe(ta)_2$ (0.26) and $Fe(cta)_2$ (0.06) should first be emphasised. Therefore, based on previous HPPXRD studies,[18] a significant smaller *B* for $Fe(ta)_2$ is expected. In contrast, the similar *B* of $Fe(ta)_2$ and $Fe(cta)_2$ imply that other factors contribute to the structural response. Looking at the evolution of Fe–N bond length in both compounds between p = ambient − 0.4 GPa, very similar relative changes of approximately 0.008% for $Fe(ta)_2$ and 0.009% for $Fe(cta)_2$ are observed despite the difference in spin-state which makes bond-compression for $Fe(ta)_2$ energetically more demanding, see ESI† for a full list of Rietveld refinement results, *i.e.* bond lengths and R_{wp} values (Tables S1 and S2). Therefore, we hypothesise that in $Fe(ta)_2$, the larger bond strength is the dominating factor, which limits the effect of the relatively low packing density. In $Fe(cta)_2$, the cyclopentyl backbone of the $(cta)^-$ linker is crowding the network, and instead of bond compression, the steric hindrance of the cyclopentyl molecules is sought to be the dominating structural feature. Notably, increased steric hindrance was recently found to lower *B*,[60] which we do not observe for $Fe(cta)_2$ in comparison to $Fe(ta)_2$. Therefore, we identify the spin-state as determining factor over steric hindrance and void fraction for the mechanical properties of Fe(II) MOFs with different Fe(II) spin-states.

Conclusion

In conclusion, we report the synthesis of two new Fe(II)-containing MOFs based on modified triazolate linkers, *i.e.* $(cta)^-$ and $(mta)^-$, which are in their high-spin states at ambient conditions. We thus show that design principles for Fe(II)-based MOFs rely on backbone modification of the linker, very much akin to what is known for SCO complexes; however, cooperative effects make property-by-design such as critical temperature of SCO and hysteresis effects very challenging. We then apply $Fe(ta)_2$ and $Fe(cta)_2$ as model systems to investigate their structural response to hydrostatic pressure, obtaining similar *B*s despite a large difference in their void fraction which was previously identified as important factor in determining the high-pressure responsiveness of MOFs. Instead, we rationalise their similar behaviours based on the interplay of several counteracting factors such as spin-state and resulting differences in Fe–N bond-strength, steric effects due to linker-backbone modification and void fraction, overall demonstrating the complexity of comprehending MOFs' response to pressure as a stimulus.

In the bigger context, as MOFs move closer to application, the interest in learning about their responsiveness to pressure will further increase. High-pressure diffraction experiments return important application-oriented properties, such as mechanical stability related to processibility concerns and material longevity. Additionally, high-pressure diffraction experiments can reveal counterintuitive effects such as negative compressibility and pressure-induced phase transitions in flexible MOFs which might initiate new actuation, energy storage, and energy dissipation technologies in the future. In all these areas, material optimisation is coupled to an in-depth knowledge of factors that contribute to the pressure-responsive properties of MOFs, a gap that is in the process of being closed since a few years – with surely many exciting discoveries to follow.

Data availability

3D electron diffraction data have been deposited in the CCDC (2311804–2311811).†

Author contributions

S. M. K.: methodology, validation, formal analysis, investigation, data curation, writing – original draft, review and editing, visualisation. R. R.: validation, formal analysis, investigation, data curation, writing – review and editing, visualisation. S. A. H., M. H., H. K., T. L., E. M., J. P., M. J. C., D. D., J. W.: investigation such as material synthesis, HPPXRD, magnetic measurements and 3DED. D. V.: conceptualisation, writing – review and editing, resources. G. K.: visualisation, conceptualisation, writing – review and editing, supervision, resources, project administration.

Conflicts of interest

There are no conflicts to declare.

Acknowledgements

The authors would like to thank the DFG for financial support (project (450070835) and project SPP 1928 COORNETs Coordination Networks: Building Blocks for Functional Systems (107745057)) and the Diamond Light Source for granting HPPXRD beamtime (CY30815-2). G. K. acknowledges support from the Heisenberg program (524525093). The authors are grateful for help with DSC measurements from Dr Robert Horny. The authors would like to thank Dr Maciej Grzywa for assistance with 3DED measurements and Shinjoo Park for assistance with Rietveld analysis.

Notes and references

1 C. L. Hobday and G. Kieslich, *Dalton Trans.*, 2021, **50**, 3759–3768.
2 A. P. Katsoulidis, D. Antypov, G. F. S. Whitehead, E. J. Carrington, D. J. Adams, N. G. Berry, G. R. Darling, M. S. Dyer and M. J. Rosseinsky, *Nature*, 2019, **565**, 213–217.
3 K. W. Chapman, G. J. Halder and P. J. Chupas, *J. Am. Chem. Soc.*, 2008, **130**, 10524–10526.
4 P. Iacomi, J. S. Lee, L. Vanduyfhuys, K. H. Cho, P. Fertey, J. Wieme, D. Granier, G. Maurin, V. van Speybroeck, J.-S. Chang and P. G. Yot, *Chem. Sci.*, 2021, **12**, 5682–5687.
5 X. Zhou, Y.-R. Miao, W. L. Shaw, K. S. Suslick and D. D. Dlott, *J. Am. Chem. Soc.*, 2019, **141**, 2220–2223.
6 G. F. Turner, S. C. McKellar, D. R. Allan, A. K. Cheetham, S. Henke and S. A. Moggach, *Chem. Sci.*, 2021, **12**, 13793–13801.
7 A. B. Cairns, J. Catafesta, C. Levelut, J. Rouquette, A. van der Lee, L. Peters, A. L. Thompson, V. Dmitriev, J. Haines and A. L. Goodwin, *Nat. Mater.*, 2013, **12**, 212–216.
8 W. Cai and A. Katrusiak, *Nat. Commun.*, 2014, **5**, 4337.
9 A. J. R. Thom, G. F. Turner, Z. H. Davis, M. R. Ward, I. Pakamorė, C. L. Hobday, D. R. Allan, M. R. Warren, W. L. W. Leung, I. D. H. Oswald, R. E. Morris, S. A. Moggach, S. E. Ashbrook and R. S. Forgan, *Chem. Sci.*, 2023, **14**, 7716–7724.
10 S. Dissegna, P. Vervoorts, C. L. Hobday, T. Düren, D. Daisenberger, A. J. Smith, R. A. Fischer and G. Kieslich, *J. Am. Chem. Soc.*, 2018, **140**, 11581–11584.
11 J. C. Tan and A. K. Cheetham, *Chem. Soc. Rev.*, 2011, **40**, 1059–1080.
12 L. R. Redfern and O. K. Farha, *Chem. Sci.*, 2019, **10**, 10666–10679.
13 S. A. Moggach and G. F. Turner, in *Mechanical Behaviour of Metal – Organic Framework Materials*, ed. J.-C. Tan, The Royal Society of Chemistry, 2023, pp. 205–266.
14 S. C. McKellar and S. A. Moggach, *Acta Crystallogr., Sect. B: Struct. Sci., Cryst. Eng. Mater.*, 2015, **71**, 587–607.
15 R. Gross and A. Marx, *Festkörperphysik*, De Gruyter Oldenbourg, 2014.
16 P. Vervoorts, J. Stebani, A. S. J. Méndez and G. Kieslich, *ACS Mater. Lett.*, 2021, **3**, 1635–1651.
17 J.-C. Tan, *Mechanical Behaviour of Metal – Organic Framework Materials*, The Royal Society of Chemistry, 2023.
18 L. R. Redfern, L. Robison, M. C. Wasson, S. Goswami, J. Lyu, T. Islamoglu, K. W. Chapman and O. K. Farha, *J. Am. Chem. Soc.*, 2019, **141**, 4365–4371.
19 C. Schneider, D. Bodesheim, J. Keupp, R. Schmid and G. Kieslich, *Nat. Commun.*, 2019, **10**, 4921.
20 L. Robison, R. J. Drout, L. R. Redfern, F. A. Son, M. C. Wasson, S. Goswami, Z. Chen, A. Olszewski, K. B. Idrees, T. Islamoglu and O. K. Farha, *Chem. Mater.*, 2020, **32**, 3545–3552.
21 P. Z. Moghadam, S. M. Rogge, A. Li, C.-M. Chow, J. Wieme, N. Moharrami, M. Aragones-Anglada, G. Conduit, D. A. Gomez-Gualdron, V. van Speybroeck and D. Fairen-Jimenez, *Matter*, 2019, **1**, 219–234.
22 L. R. Redfern, M. Ducamp, M. C. Wasson, L. Robison, F. A. Son, F.-X. Coudert and O. K. Farha, *Chem. Mater.*, 2020, **32**, 5864–5871.
23 S. M. J. Rogge, P. G. Yot, J. Jacobsen, F. Muniz-Miranda, S. Vandenbrande, J. Gosch, V. Ortiz, I. E. Collings, S. Devautour-Vinot, G. Maurin, N. Stock and V. van Speybroeck, *ACS Mater. Lett.*, 2020, **2**, 438–445.
24 R. Li, G. Levchenko, F. J. Valverde-Muñoz, A. B. Gaspar, V. V. Ivashko, Q. Li, B. Liu, M. Yuan, H. Fylymonov and J. A. Real, *Inorg. Chem.*, 2021, **60**, 16016–16028.
25 I. R. Reddy, P. M. Oppeneer and K. Tarafder, *J. Magn. Magn. Mater.*, 2021, **524**, 167637.
26 R. Li, V. M. Kalita, H. Fylymonov, W. Xu, Q. Li, J. A. Real, B. Liu and G. Levchenko, *Inorg. Chem.*, 2022, **61**, 14752–14760.
27 D. Paliwoda, L. Vendier, L. Getzner, F. Alabarse, D. Comboni, B. Martin, S. E. Alavi, M. P. Bello, L. Salmon, W. Nicolazzi, G. Molnár and A. Bousseksou, *Cryst. Growth Des.*, 2023, **23**, 1903–1914.
28 M. Mikolasek, M. D. Manrique-Juarez, H. J. Shepherd, K. Ridier, S. Rat, V. Shalabaeva, A.-C. Bas, I. E. Collings, F. Mathieu, J. Cacheux, T. Leichle, L. Nicu, W. Nicolazzi, L. Salmon, G. Molnár and A. Bousseksou, *J. Am. Chem. Soc.*, 2018, **140**, 8970–8979.
29 M. Grzywa, R. Röß-Ohlenroth, C. Muschielok, H. Oberhofer, A. Błachowski, J. Żukrowski, D. Vieweg, H.-A. K. von Nidda and D. Volkmer, *Inorg. Chem.*, 2020, **59**, 10501–10511.
30 F. Gándara, F. J. Uribe-Romo, D. K. Britt, H. Furukawa, L. Lei, R. Cheng, X. Duan, M. O'Keeffe and O. M. Yaghi, *Chem. – Eur. J.*, 2012, **18**, 10595–10601.
31 X.-H. Zhou, Y.-H. Peng, X.-D. Du, J.-L. Zuo and X.-Z. You, *CrystEngComm*, 2009, **11**, 1964.
32 M. Grzywa, D. Denysenko, J. Hanss, E.-W. Scheidt, W. Scherer, M. Weil and D. Volkmer, *Dalton Trans.*, 2012, **41**, 4239–4248.
33 J. G. Park, B. A. Collins, L. E. Darago, T. Runčevski, M. E. Ziebel, M. L. Aubrey, H. Z. H. Jiang, E. Velasquez, M. A. Green, J. D. Goodpaster and J. R. Long, *Nat. Chem.*, 2021, **13**, 594–598.
34 R. P. Nutakki, R. Röß-Ohlenroth, D. Volkmer, A. Jesche, H.-A. K. von Nidda, A. A. Tsirlin, P. Gegenwart, L. Pollet and L. D. C. Jaubert, *Phys. Rev. Res.*, 2023, **5**, L022018.
35 C. Muschielok, A. Reiner, R. Röß-Ohlenroth, A. Kalytta-Mewes, D. Volkmer, A. Wixforth and H. Oberhofer, *ACS Appl. Mater. Interfaces*, 2022, **14**, 33662–33674.
36 J. G. Park, M. L. Aubrey, J. Oktawiec, K. Chakarawet, L. E. Darago, F. Grandjean, G. J. Long and J. R. Long, *J. Am. Chem. Soc.*, 2018, **140**, 8526–8534.
37 A. B. Andreeva, K. N. Le, K. Kadota, S. Horike, C. H. Hendon and C. K. Brozek, *Chem. Mater.*, 2021, **33**, 8534–8545.
38 M. C. Demuth, K. N. Le, M. Sciprint and C. H. Hendon, *J. Phys. Chem. C*, 2023, **127**, 2735–2740.
39 Y. Garcia, V. Niel, M. C. Muñoz and J. A. Real, *Spin crossover in transition metal compounds*, Springer, Berlin, 2004, pp. 229–257.
40 D. Boldrin, *Appl. Phys. Lett.*, 2021, **118**, 170502.
41 J. Wieme, S. M. J. Rogge, P. G. Yot, L. Vanduyfhuys, S.-K. Lee, J.-S. Chang, M. Waroquier, G. Maurin and V. van Speybroeck, *J. Mater. Chem. A*, 2019, **7**, 22663–22674.

42 J. Thomas, S. Jana, S. Liekens and W. Dehaen, *Chem. Commun.*, 2016, **52**, 9236–9239.
43 P. R. Clark, G. D. Williams, J. F. Hayes and N. C. O. Tomkinson, *Angew. Chem., Int. Ed.*, 2020, **59**, 6740–6744.
44 M. A. Hoselton, L. J. Wilson and R. S. Drago, *J. Am. Chem. Soc.*, 1975, **97**, 1722–1729.
45 A. L. Spek, *J. Appl. Crystallogr.*, 2003, **36**, 7–13.
46 N. J. Brooks, B. L. L. E. Gauthe, N. J. Terrill, S. E. Rogers, R. H. Templer, O. Ces and J. M. Seddon, *Rev. Sci. Instrum.*, 2010, **81**, 64103.
47 G. P. Robertson, S. Mosca, C. Castillo-Blas, F. A. Son, O. K. Farha, D. A. Keen, S. Anzellini and T. D. Bennett, *Inorg. Chem.*, 2023, **62**, 10092–10099.
48 S. Grover, S. Burger, K. T. Butler, K. Hemmer, P. Vervoorts, G. Kieslich and R. Grau-Crespo, *CrystEngComm*, 2023, **25**, 3439–3444.
49 A. J. Graham, D. R. Allan, A. Muszkiewicz, C. A. Morrison and S. A. Moggach, *Angew. Chem., Int. Ed.*, 2011, **50**, 11138–11141.
50 K. W. Chapman, G. J. Halder and P. J. Chupas, *J. Am. Chem. Soc.*, 2009, **131**, 17546–17547.
51 P. Vervoorts, J. Keupp, A. Schneemann, C. L. Hobday, D. Daisenberger, R. A. Fischer, R. Schmid and G. Kieslich, *Angew. Chem., Int. Ed.*, 2021, **60**, 787–793.
52 Y. H. Hu and L. Zhang, *Phys. Rev. B: Condens. Matter Mater. Phys.*, 2010, **81**, 174103.
53 J. Gonzalez-Platas, M. Alvaro, F. Nestola and R. Angel, *J. Appl. Crystallogr.*, 2016, **49**, 1377–1382.
54 M. J. Cliffe and A. L. Goodwin, *J. Appl. Crystallogr.*, 2012, **45**, 1321–1329.
55 P. Vervoorts, C. L. Hobday, M. G. Ehrenreich, D. Daisenberger and G. Kieslich, *Z. Anorg. Allg. Chem.*, 2019, **645**, 970–974.
56 M. T. Wharmby, F. Niekiel, J. Benecke, S. Waitschat, H. Reinsch, D. Daisenberger, N. Stock and P. G. Yot, *Nanomaterials*, 2020, **10**, 1698.
57 A. U. Ortiz, A. Boutin, A. H. Fuchs and F.-X. Coudert, *J. Chem. Phys.*, 2013, **138**, 174703.
58 W. W. Schmahl, I. P. Swainson, T. Dove and A. Graeme-Barber, *Z. Kristallogr. – Cryst. Mater.*, 1992, **201**, 125–146.
59 K. D. Hammonds, M. T. Dove, A. P. Giddy, V. Heine and B. Winkler, *Am. Mineral.*, 1996, **81**, 1057–1079.
60 F. A. Son, K. M. Fahy, M. A. Gaidimas, C. S. Smoljan, M. C. Wasson and O. K. Farha, *Commun. Chem.*, 2023, **6**, 185.

